Control Engineering Practice 29 (2014) 277–286

Contents lists available at ScienceDirect

Control Engineering Practice

journal homepage: www.elsevier.com/locate/conengprac

Hardware-in-the-loop validation of a power management strategy for hybrid powertrains

Youngki Kim [a], Ashwin Salvi [a], Jason B. Siegel [a], Zoran S. Filipi [b], Anna G. Stefanopoulou [a], Tulga Ersal [a,*]

[a] Mechanical Engineering, University of Michigan, 1231 Beal Ave., Ann Arbor, MI 48109, United States
[b] Automotive Engineering, Clemson University, Greenville, SC 29607, United States

ARTICLE INFO

Article history:
Received 15 May 2013
Accepted 22 April 2014
Available online 2 June 2014

Keywords:
Hardware-in-the-loop simulation
Power management
Hybrid electric vehicles
Optimization
Validation

ABSTRACT

Previously, a hybrid powertrain management strategy was developed that controls the power sources based on frequency content, mitigating aggressive engine transients. This article presents a hardware-in-the-loop validation of this strategy, with a real engine and battery integrated into a diesel hybrid electric vehicle simulation, thereby allowing for a realistic evaluation of fuel economy, soot emissions, and battery life. Considering an aggressive drive cycle and a state-of-charge regulation strategy as a benchmark, the frequency-based strategy yields 5.9% increase in fuel economy, 62.7% decrease in soot emissions, and 23% reduction in effective Amp-hours processed, which should yield an increase in battery life.

1. Introduction

Vehicle powertrain hybridization is one of the promising pathways for improved fuel economy and reduced tailpipe emissions, where energy storage devices, such as hydraulic or pneumatic accumulators or batteries, are used in conjunction with internal combustion engines. Various topologies for hybridization have been explored; e.g., series (Filipi & Kim, 2010; Jalil, Kheir, & Salman, 1997), parallel (Liu, Hagena, Peng, & Filipi, 2008; Yang, Qi, Guo, Wang, & Wei, 2012), and power split (or series–parallel) (Li & Kar, 2011; Liu & Peng, 2008). They all demonstrated improvements in fuel economy and some showed reduction in emissions.

Hybrid powertrain technology has already been successfully deployed on some passenger vehicles (Lave & MacLean, 2002). Heavy-duty military vehicles could benefit from this technology, as well. Even though they have significantly different performance requirements and driving patterns than those of the passenger vehicles, the goals of reducing fuel consumption and emissions are still the same. Minimizing soot emissions is extremely desirable within the military context to reduce the vehicle visual signature and increase survivability. Further requirements such as silent watch, increased mobility, enhanced functionality for on-board power, and improved export-power capabilities make hybrid electric configurations more attractive than other hybrid architectures. Among various hybrid electric configurations, the series configuration has drawn interest due to greater flexibility in vehicle design when it comes to considerations such as the V-shaped hull design to maximize the survivability of the crew during blast events (Ramasamy, Hill, Hepper, Bull, & Clasper, 2009). Therefore, with the specific military application in mind, the focus of this article is on the series hybrid electric architecture.

The performance of a hybrid powertrain in terms of reducing both fuel consumption and emissions critically depends on the power management strategy; that is, the supervisory control algorithm that determines how the total power demanded by the driver will be shared between the engine and, for example, the battery. Many power management strategies for series hybrid electric vehicles have been proposed to fully exploit their potential for minimizing fuel consumption, emissions, and/or battery health (Caratozzolo, Serra, & Riera, 2003; Di Cairano, Liang, Kolmanovsky, Kuang, & Phillips, 2012; Jalil et al., 1997; Kim & Filipi, 2007; Kim, Lee, & Filipi, 2012; Konev, Lezhnev, & Kolmanovsky, 2006; Li & Feng, 2012; Michel et al., 2013; Pisu & Rizzoni, 2005; Serrao, Onori, Sciarretta, Guezennec, & Rizzoni, 2011, 2013).

Among many strategies proposed, Konev et al. and Di Cairano et al. highlight the importance of a smooth engine operation, where smoothness is characterized by the rate of change in power. Depending on the engine specifications, different rate of change thresholds can be used to define the smooth operation threshold.

* Corresponding author. Tel.: +1 734 763 7388.
E-mail addresses: youngki@umich.edu (Y. Kim), asalvi@umich.edu (A. Salvi), siegeljb@umich.edu (J.B. Siegel), zfilipi@clemson.edu (Z.S. Filipi), annastef@umich.edu (A.G. Stefanopoulou), tersal@umich.edu (T. Ersal).

http://dx.doi.org/10.1016/j.conengprac.2014.04.008
0967-0661/

Smooth operation is important for two reasons: (1) it allows the engine to operate close to the steady-state conditions where the operation is optimal in terms of pointwise powertrain efficiency; and (2) reducing aggressive transients also reduces soot emissions. To achieve such smooth operation, Konev et al. and Di Cairano et al. propose methods to smoothen the power demand that is required from the engine. In their work, Konev et al. and Di Cairano et al. focus on the benefits of this strategy from the engine perspective only and within the context of passenger vehicles with spark-ignition engines. Serrao et al. developed a power management strategy accounting for tailpipe emissions such as NO_x in Serrao et al. (2013); however, soot emissions – a significant factor in military vehicles – were not considered. Therefore, the impact of this strategy within the context of military vehicles with diesel engines is still an open-research question. Furthermore, the impact of engine power smoothing strategy on the battery operation and battery health has yet to be studied. Michel et al. accounted for the battery thermal behavior in the equivalent consumption minimization strategy in Michel et al. (2013) where battery health was indirectly considered based on knowledge that capacity fade can be accelerated at high temperatures; however, the battery life estimation was not conducted. Thus, this article is aimed to investigate the effects of a power-smoothing strategy in a series hybrid electric military vehicle with a diesel engine. The effects are addressed from the perspective of both the engine and the battery.

Towards this end, a frequency-domain power distribution (FDPD) strategy is considered that has been proposed by Kim, Lee, et al. (2012). The FDPD strategy manages power flow by splitting power demand into low and high frequency components through low-pass filtering incorporated with load-leveling. Model-based simulations have shown the method to be capable of achieving: (1) reduced battery electric loads, (2) smooth engine transients; and (3) less fuel consumption. However, a method to tune the FDPD has not yet been proposed. Furthermore, the simulation-based validations were performed with static maps to represent the engine and its emissions. The true transient performance of FDPD with real hardware has not yet been studied.

With this motivation in mind, this article makes two original contributions to this body of literature. First, it provides a design methodology to tune the frequency-based supervisory controller. Control parameters are systematically optimized through a model-based two-stage optimization process. Second, the FDPD strategy is evaluated experimentally through a networked simulation setup with a real engine and battery in the loop. This hardware-in-the-loop simulation allows not only for a more realistic evaluation of the fuel economy benefits of the controller compared to the purely model based evaluations in the literature, but also for an assessment of its soot emissions benefits for the first time. In addition, the battery life is estimated using a weighted Amp-hour (Ah) processed model (Onori, Spagnol, Marano, Guezennec, & Rizzoni, 2012; Serrao, Onori, Rizzoni, & Guezennec, 2009) to account for thermal effects. A thermostatic control strategy is also considered as a baseline power management strategy, and the FDPD is compared to the baseline strategy in terms of performance. This article is based upon the preliminary work reported in Kim, Ersal, Salvi, Stefanopoulou, and Filipi (2012) and extends it by putting a real battery in the loop in addition to the engine and by providing emissions measurements, as well. A more detailed estimation of the battery life is also included.

The rest of this article is organized as follows. Section 2 gives an overview of the power management strategies considered in this article and also proposes a method to tune the FDPD strategy. Section 3 presents the vehicle system considered as a case study and optimized control parameters. Hardware-in-the-loop setup and experimental results are presented and discussed in Section 4, and conclusions are drawn in Section 5.

2. Overview of power management strategies

The primary task of a power management strategy (PMS) is determining the power flow between the vehicle, engine and battery to minimize a cost function such as fuel consumption and emissions. Specifically, a series hybrid configuration can take advantage of the decoupling of the engine from the wheels to operate the engine at the optimal conditions. However, the decrease in total system efficiency due to inherent multiple energy conversions, and other constraints such as battery voltage and current limitations make the power management problem a challenging task. Therefore, the design of power management strategy is important to improve fuel economy while reducing engine emissions and to ensure safe battery operations.

2.1. Thermostatic battery state-of-charge (SOC) control

Thermostatic SOC control, a heuristic control technique, has been widely employed for series hybrid electric vehicles (Caratozzolo et al., 2003; Lee et al., 2011; Li & Feng, 2012). This strategy is advantageous because of its ease of implementation, the effectiveness of SOC regulation, and improved fuel economy. Thus, the thermostatic SOC control is considered as a baseline strategy in this study.

Fig. 1 summarizes the principle of the thermostatic SOC control. As long as current SOC is higher than the target SOC, the engine provides zero power. The engine starts charging the battery with the predetermined power level when SOC drops to the target SOC. A dead band is implemented to prevent frequent engine on/off's. When the power demand for vehicle propulsion is higher than the battery discharging power limit, the engine operates in power assisting mode.

However, the thermostatic SOC control has several drawbacks. Since the engine is commanded to provide power demand above threshold level, the engine operation changes suddenly and aggressively from zero power demand. This behavior considerably deteriorates tailpipe emissions (Hagena, Assanis, & Filipi, 2011) and also prevents the engine from following the optimal operation line (Di Cairano et al., 2012). Moreover, the heavy-duty diesel engine cannot follow the aggressive command because of its large inertia and turbo-charger lag. This is a problem because the battery has to provide the remainder of the power demand, resulting in more electrochemical–mechanical stresses in the battery (Lee, Kim, Stefanopoulou, & Filipi, 2011). Finally, in terms of improving the fuel economy, this strategy cannot avoid multiple power conversions since it prefers using the battery power to the engine/generator power.

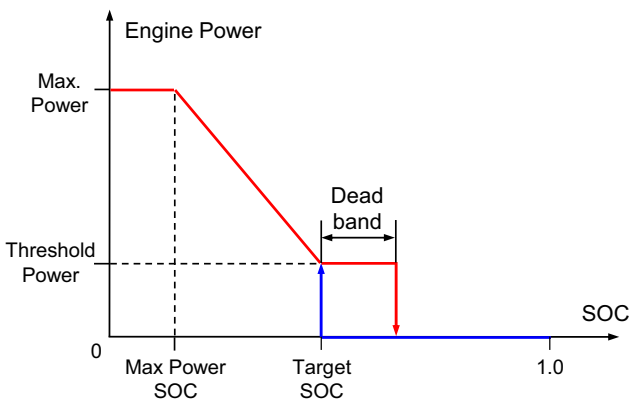

Fig. 1. The schematic of thermostatic SOC control.

2.2. Frequency domain power distribution strategy

The separation of power demand in frequency domain provides control inputs to each power source tailored according to speed of response. Unlike the turbo-charged diesel engine, the battery can absorb and provide high frequency power demands without delay in response. Therefore, by splitting the total power demand into low frequency and high frequency components, each power source can be utilized more effectively. The low frequency components capture the smooth trajectory of the power demand, whereas the high frequency components cover the small amplitude but aggressive and transient power demand. The smooth power demand transitions can help reduce engine emissions, whereas the reduced amplitude of the electric load is beneficial to mitigate electrical stress on the battery which will be discussed in Section 4.

Fig. 2 shows the structure of the proposed strategy consisting of: (1) FDPD module; (2) SOC regulation module; and (3) mode decision module. The FDPD module for the hybrid electric vehicle (HEV) mode determines the engine/generator power demand by splitting the total power demand into low and high frequency components. The power demand $P_{dmd,1}$ is determined as follows:

Algorithm 1.

if $P_{th,1} \le P_{dmd,0} \le P_{th,2}$ **then**
  $P_{dmd,1} = P_{dmd,0} + \Delta P_{dmd}$
else if $P_{dmd,0} > P_{th,2}$ **then**
  $P_{dmd,1} = P_{th,2} + \Delta P_{dmd}$
else
  $P_{dmd,1} = \Delta P_{dmd}$
end

where $P_{dmd,0}$ and $P_{dmd,1}$ are power demand for vehicle propulsion and total power demand respectively. Parameters P_{th1} and P_{th2} are threshold power levels for HEV mode incorporated with load-leveling, and τ_{LF} is the time constant of a low-pass filter. Then, the power demand $P_{dmd,2}$ is filtered using a first order low-pass filter:

$$\tau_{LF}\frac{dP_{dmd,2}}{dt} + P_{dmd,2} = P_{dmd,1}. \quad (1)$$

A first order filter is used in this study since a first-order filter outperforms higher order filters in terms of fuel economy and engine smoothness as suggested by Kim, Lee, et al. (2012).

The feedback power demand ΔP_{dmd} for the battery SOC regulation is determined through the proportional-integral (PI) controller given by

$$\Delta P_{dmd} = k_P \Delta \mathrm{SOC} + k_I \int \Delta \mathrm{SOC}\, dt, \quad (2)$$

where ΔSOC is the difference between the current and reference SOC values; k_P and k_I are proportional and integral control gains respectively.

The mode decision module determines driving modes. The modes change between an electric-vehicle (EV) mode, a hybrid electric vehicle (HEV) mode and a performance vehicle (PV) mode according to the following:

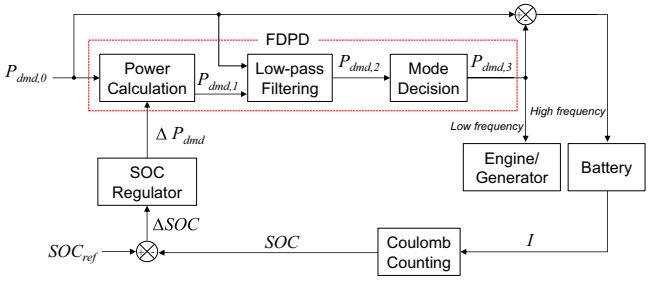

Fig. 2. The schematic diagram of the FDPD strategy.

Algorithm 2.

if $P_{dmd,2} \le P_{th,1}$ **then**
  $P_{dmd,3} = 0$: EV mode
else
  if $P_{dmd,2} \ge P_{dmd,0} - P_{batt,max}$ **then**
    $P_{dmd,3} = P_{dmd,2}$: HEV mode
  else
    $P_{dmd,3} = \min(P_{eng,max}, P_{dmd,0} - P_{batt,max})$: PV mode
  end
end

where $P_{eng,max}$ and $P_{batt,max}$ are the maximum available engine power and battery discharging power, respectively. Consequently, the performance of FDPD strategy is determined by five control parameters; namely, τ_{LF}, P_{th1}, P_{th2}, k_P, and k_I. These five parameters are determined through a model-based two-stage optimization process as described next.

2.3. Model-based control parameter optimization

In this section, the formulation of the optimization of control parameters for the thermostatic and FDPD strategies using a model-based simulation is presented. A hybrid vehicle is a complicated system that includes both energy conversion and energy storage among various power/energy sources. Since numerical round-off, interpolation inaccuracy, and discrete events in the vehicle simulation lead to discontinuity and computational noise in the objective function (Assanis et al., 1999; Gao & Porandla, 2005), gradient-based optimization algorithms are not frequently used. Thus, a two-stage optimization framework was used in this study to take advantage of both derivative-free (global) and gradient-based (local) optimization algorithms. First, a non-gradient based optimization algorithm searches for the global minimum over a bounded domain. Then, the set is used as an initial point for a gradient-based algorithm with fast convergence. The DIviding RECTangles (DIRECT) algorithm is used for the global optimization, wherein the feasible region of design variables is divided into n-dimensional hyper-cubes and hyper-rectangles and the objective function is evaluated at the center of the hyper-cubes and hyper-rectangles. This algorithm has several advantages (Jones, Perttunen, & Stuckman, 1993): (1) it searches for global and local optima; (2) parameter tuning is not required; (3) both equality and inequality constraints can be easily handled; (4) it is robust for nonlinear problems. For the subsequent local optimization algorithm, Sequential Quadratic Programming (SQP) is used. Both DIRECT and SQP are implemented in MATLAB through the *gclsolve.m* code by Holmstrom (1989) and the built-in MATLAB function *fmincon*, respectively.

The control parameter optimization can be mathematically formulated as the following:

$$\begin{aligned} &\text{Objective}: \quad \text{Maximize fuel economy} \\ &\text{Subject to} \quad |\Delta v_{veh}| \le \Delta v_{veh,ref} \text{ within 1 s} \\ &\qquad\qquad \mathrm{SOC}_L \le \mathrm{SOC} \le \mathrm{SOC}_U \\ &\qquad\qquad \mathrm{SOC}_{end,L} \le \mathrm{SOC}_{end} \le \mathrm{SOC}_{end,U} \\ &\qquad\qquad P(\dot{P}_{eng} \le \alpha) \ge \beta \end{aligned}$$

where the subscripts *ref* and *end* represent the reference and the end of driving cycles and the subscripts L and U denote the lower and upper bounds, respectively. The difference between the desired and actual vehicle speeds is represented by Δv_{veh} and

$\Delta v_{veh,ref}$ is set to 1.6 km/h based on the regulation of US Environmental Protection Agency (EPA).[1] The SOC should be bounded during the vehicle operation and the SOC at the end of the driving cycle should be sufficiently close to the target SOC. The variable $\dot{P}_{eng}$ is the derivative of engine power demand with respect to time; thus, the last constraint can be interpreted as a minimum probability of β for an engine power command rate less than α. The parameters α and β are set to 40 kW/s and 95% adopted from Kim, Lee, et al. (2012). For the purpose of accounting for the remaining battery SOC, two consecutive driving cycles are considered; the fuel economy is calculated by

$$\text{fuel economy} = \frac{1}{N_s}\sum_{k=1}^{N_s}\frac{\int_{t_k}^{t_k+t_{\text{cycle}}} v_{\text{veh}}\,dt}{\int_{t_k}^{t_k+t_{\text{cycle}}} \dot{m}_f\,dt}, \tag{3}$$

where t_{cycle} is the total time of the given driving cycle, v_{veh} is the velocity of the vehicle and N_s is the total number of t_k's that satisfy the condition: $t_k \ni \text{SOC}(t_k) = \text{SOC}(t_k + t_{\text{cycle}})$.

The same optimization formulation is used to tune both the thermostatic SOC and FDPD control strategies.

3. Description of the hardware-in-the-loop study

As a case study, a hybridized Mine Resistant Ambush Protected All-Terrain Vehicle (M-ATV) is considered to explore the effectiveness of the FDPD strategy in severe circumstances including frequent and high power demand. The specifications of the M-ATV are summarized in Table 1.

A networked hardware-in-the-loop simulation (Ersal et al., 2011; Ersal, Brudnak, Stein, & Fathy, 2012; Ersal, Gillespie, Brudnak, Stein, & Fathy, 2013) of this vehicle system is considered to enable a system integration despite the fact that the components resided in different geographic locations. The engine and battery are the hardware components located in two different locations, and the remaining components of the vehicle system (i.e., generator, motors, vehicle dynamics, and driver) are mathematically modeled and simulated in a third location to enable a future study with a human driver in the loop setup at a location not collocated with the engine or battery similar to Ersal et al. (2011). One of the important considerations in such networked simulation is selecting the location of the coupling point – how to distribute the models between the sites (Ersal et al., 2013). The coupling point significantly affects how the system dynamics are affected by the network dynamics (e.g., delay). To this end, for the three-site networked setup considered in this work, there are three options for where the PMS can be placed: with the driver, battery, or engine. Among these three options, placing the PMS with the driver is advantageous, because this is the only option which does not require a third communication channel between the engine and battery locations. Working with only two communication channels (between the driver site and the engine site, and between the driver site and the battery site) decreases the sensitivity of the simulation to communication delays.

More details about the SHEV model are described in Appendix A. The overview of the networked system architecture is illustrated in Fig. 3.

3.1. Engine-in-the-loop setup

A Navistar 6.4 L V8 diesel engine with 260 kW rated power at 3000 rpm and a rated torque of 880 N m at 2000 rpm is used for this study. It is intended for a variety of medium-duty truck applications covering the range between classes IIB and VII, and features technologies such as high pressure common rail fuel injection, twin sequential turbochargers, and exhaust gas recirculation. A high-fidelity, AC electric dynamometer couples the physical engine with the simulation models in real time and operates in speed control mode. The setup is connected to Matlab/Simulink for integration with mathematical models, allowing for a real-time hardware-in-the-loop simulation. This connection is achieved through an EMCON 400 flexible test bed with an ISAC 400 extension (Filipi et al., 2006). The photo of the engine-in-the-loop setup is shown in Fig. 4.

Transient soot emissions are measured with a Differential Mobility Spectrometer (DMS) 500 manufactured by Cambustion Ltd. in the form of temporally resolved particulate concentrations. The DMS 500, whose measurement principle is illustrated in Fig. 5, offers measurement of different particle sizes by identifying the mobility of particles with a sampling frequency of 10 Hz and a response time of 200 ms. Therefore, the DMS 500 makes it possible to analyze the time evolution of the soot emissions. In this study we consider a military application and thus focus on engine out emissions due to the fact that military vehicles do not use aftertreatment systems. Soot emission measurements are performed for a time window of 750 s due to the limitation of the measurement instrument for reliable and repeatable data. After 750 s, the measurements start becoming unreliable due to contamination in the instrument.

Table 1
Vehicle specification.

Parameter	Value	Unit
Weight	14 403	kg
Payload	1814	kg
Frontal area	5.72	m^2
Diesel engine	260	kW
Generator	236	kW
Battery	9.27	kWh
Motor	380	kW

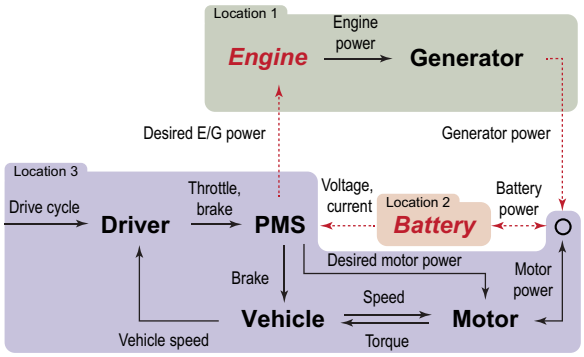

Fig. 3. The overview of the networked hardware-in-the-loop simulation setup. Each shaded area represents a different geographic location. Italic typeface denotes actual hardware components. Dashed lines represent the signals communicated over the network. PMS stands for the power management strategy.

3.2. Battery-in-the-loop setup

A cylindrical 26650 power cell manufactured by A123 systems is used for the battery-in-the-loop test. The cell chemistry is LFP with capacity of 2.3 Ah. The specifications of the battery pack and cell are summarized in Table 2. Since a single cell is tested, the battery current (or demand) requested by the power management strategy I_{pack} has to be scaled down to the cell level I_{cell} given by $I_{cell} = I_{pack}/n_p$. This scaled current demand is applied to the battery

[1] EPA, Code of Federal Regulations, Title 40 Chapter I, §600.109-08 EPA driving cycles.

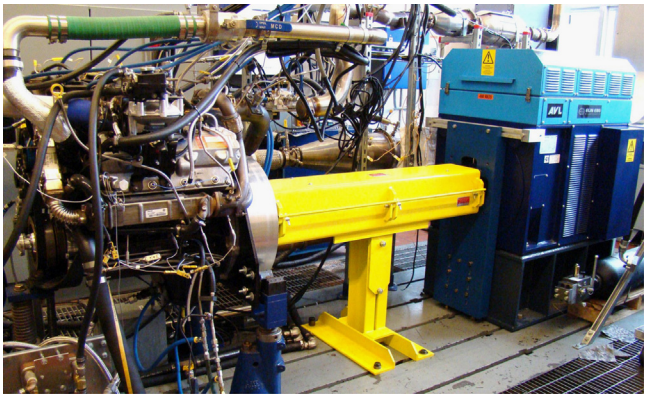

Fig. 4. A photo of the engine-in-the-loop testing facility. The engine is on the left, and the dynamometer is on the right.

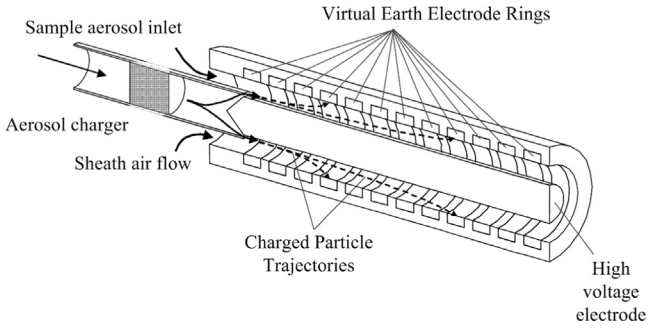

Fig. 5. The schematic of the measurement principle of the DMS system (Reavell, Hands, & Collings, 2002).

Table 2
Specifications of battery pack and cell.

	Symbol	Value
Pack		
Number of cells in series	n_s	130
Number of cells in parallel	n_p	10
Cell		
Nominal capacity	C_b	2.3 Ah
Nominal voltage	V_n	3.3 V

cell using a Bitrode Battery Test System FTV1-200/50/2-60. The battery SOC is estimated based on coulomb counting given by

$$\frac{dSOC}{dt} = -\frac{I_{cell}}{3600C_b} \tag{4}$$

where I and C_b are current and battery capacity respectively.

As seen from Fig. 6, the battery cell is placed in a designed flow chamber which emulates forced-air cooling conditions inside the battery pack (or module). Since the flow chamber is located in a thermal chamber, the ambient temperature can be controlled around a predetermined temperature at 25 °C. In particular, forced-air cooling is performed by controlling the fan speed and temperature inside the thermal chamber. To investigate the performance of different power management strategies in terms of battery life, the temperature of the battery during operation is also measured using a T-type thermocouple. The sensor accuracy is the maximum of 0.5 °C or 0.4% according to technical information from the manufacturer. Similar to the engine-in-the-loop setup, the battery-in-the-loop setup is also interfaced to Matlab/Simulink for a real-time hardware-in-the-loop simulation.

4. Experimental results and discussion

The performances of the two power management strategies are investigated using an aggressive military driving cycle, *Urban Assault Cycle* (UAC) (Lee et al., 2011), which features frequent acceleration and deceleration events. The velocity profile of this driving cycle is displayed in Fig. 7. The parameters of the baseline thermostatic SOC and the FDPD strategies, both optimized for the UAC, are summarized in Tables 3 and 4. Note that the baseline strategy behaves like proportional control above the threshold power of 20 kW; that is, the engine power increases by 34.3 kW to compensate for every 0.01 decrease in battery SOC. Fig. 8 shows the power spectral analysis of the UAC and the cut-off frequency τ_{LF} obtained as a result of the optimization.

To highlight the performance of the power management strategies, specific time periods are shown in Fig. 9. There is no difference in vehicle speed between the FDPD and thermostatic strategies, implying that the vehicle performance is not deteriorating. The engine power demand gradually changes under the FDPD strategy when the power demand is higher than 116.7 kW, the threshold power level 2, $P_{th,2}$. In general, the actual engine power can track the desired engine power very closely, indicating that the engine can operate very close to the optimal operation line. In contrast, the baseline thermostatic SOC strategy always commands engine power demand above the threshold level of 20 kW with high power rate. Moreover, it can be seen that the diesel engine cannot follow an aggressive command with high power rate due to its slow dynamics; therefore, the battery has to provide the remaining propulsion power until the engine power demand is satisfied. The thermostatic SOC strategy requires significantly high power demand to charge the battery for SOC regulation. On the other hand, the FDPD strategy reduces the power demands higher than threshold power level 2, leading to a reduced occurrence of aggressive transients. Specifically, these smooth engine transients under the FDPD strategy result in 62.7% reduction in the accumulated soot emissions from 0.822 g/km to 0.306 g/km for the first 750 s.

Furthermore, the FDPD strategy does not emphasize battery charging as much as the thermostatic SOC strategy does. The decrease in multiple power conversions could improve system efficiency. Specifically, the fuel economy is improved by 5.9% from 2.87 km/l to 3.04 km/l compared to the thermostatic SOC strategy over the UAC. The term N_s used in the fuel economy calculation in Eq. (3) is found to be 166 and 49 for the thermostatic and FDPD strategies, respectively.

Fig. 10 shows the histogram of battery cell operation and engine operation with the two power management strategies. The frequency of high battery currents and aggressive engine power demands (as quantified by the engine power rate) are significantly reduced in case of the FDPD strategy, leading to the decrease in soot emissions. Specifically, the amount of time the battery spends in high C-rate (more than ± 5 C) is reduced from 25% to 18% with the FDPD strategy. A C-rate is a measure of the rate at which a battery is discharged relative to its maximum capacity. A 1C rate means that the discharge current will discharge the entire battery in 1 h. Additionally, the high power rate (more than 50 kW/s) operation time of the engine is reduced from 51% to 1%. Since Joule heating dominates the heat generation from the battery as discussed in Kim et al. (2014), a lower operating temperature of the battery is expected corresponding to lower average C-rate. Indeed, Fig. 11 shows that the battery temperature is 3 °C lower with the FDPD than the thermostatic strategy for the same cooling condition, even though both strategies regulate the battery SOC around the target value of 0.5. These results could lead to an additional benefit of a reduction in power/energy consumption for battery cooling.

Battery degradation over the driving cycle is estimated by using the weighted Ah-processed model discussed in Onori et al. (2012). This

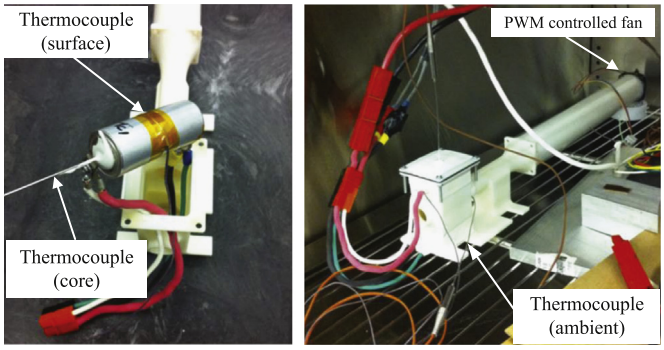

Fig. 6. A photo of the battery-in-the-loop testing facility.

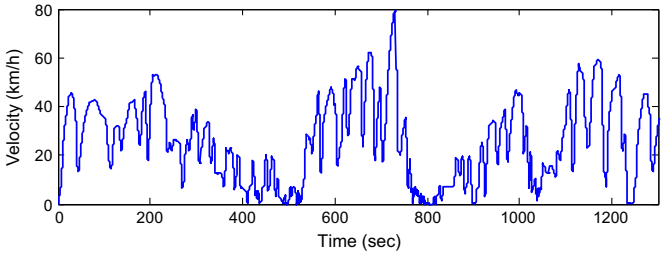

Fig. 7. The speed profile of the *Urban Assault Cycle*.

Table 3
Parameters of the thermostatic SOC strategy optimized for the UAC.

Parameter	Value	Unit
Target SOC	0.5	–
Deadband	0.02	–
Max. power SOC	0.43	–
Max. power	260	kW
Threshold power	20	kW

Table 4
Control parameters of the FDPD strategy optimized for the UAC.

Parameter	Value	Unit
Cut-off frequency, τ_{LF}	0.21	Hz
Threshold power 1, $P_{th,1}$	16.7	kW
Threshold power 2, $P_{th,2}$	116.7	kW
Proportional gain, k_P	836.2	–
Integral gain, k_I	4.537	–

approach uses the linear cumulative damage concept to analyze battery degradation. To account for the influence of operating conditions such as temperature T_{batt} and state-of-charge (SOC) or depth-of-discharge (DOD) on the degree of degradation, Onori et al. introduced the severity factor σ, a nonlinear function of battery temperature and SOC. The effective accumulated Ah-processed is calculated by using

$$\mathrm{Ah}_{\mathrm{eff}} = \int \sigma(T_{\mathrm{batt}}, \mathrm{SOC})|I|\, dt. \tag{5}$$

Even though the severity factor is highly dependent on battery specifications such as chemistry and electrode design, it is suggested that the severity factor has a typical shape as illustrated in Fig. 12 (Onori et al., 2012). As seen from Fig. 11, the operating range of the battery SOC under both strategies is narrow. Thus, it is reasonable to assume that the severity factor is only a function of temperature. By using the severity factor as a first approximation, the FDPD provides

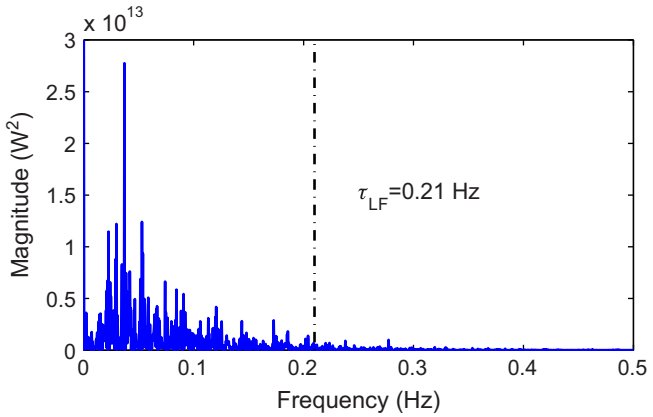

Fig. 8. Power spectral density of the power demand of the UAC.

a 23% reduction of Ah-processed over the UAC compared to the thermostatic SOC strategy. This significant decrease in the Ah-processed can be interpreted as less electrical stress on the battery and longer battery life.

In this work, the power management strategies are optimized and evaluated for one particular drive cycle. Other drive cycles may need different control gains and lead to different savings in terms of fuel economy, soot emissions, and battery life. Therefore, the presented control gains should not be interpreted as a single set of gains recommended for all drive cycles. The typical approach in the literature to ensure a robust performance is to tune the controller for different types of drive cycles separately and using a pattern recognition algorithm to switch between the best gains (Murphey et al., 2012, 2013). However, developing such a gain scheduling approach and evaluating the robustness of its performance is beyond the scope of this article and is left as future work.

5. Conclusions

The original contributions of this article can be summarized as follows. A control parameter tuning strategy has been proposed for the frequency-domain power distribution (FDPD) strategy. Control parameters are systematically determined through the model-based two-stage optimization process, where non-gradient and gradient based algorithms are sequentially combined to take advantage of both algorithms.

A case study has been conducted to experimentally compare the performance of the FDPD to the thermostatic SOC strategy as the baseline. A networked hardware-in-the-loop simulation platform has been developed for this purpose and a Mine Resistant Ambush Protected All-Terrain Vehicle (M-ATV) has been considered as the vehicle system.

The results show that the FDPD strategy successfully reduces aggressive engine power demand and excessive electric battery loads while improving fuel economy by 5.9% compared to the baseline strategy in the specific scenario considered. The smooth engine power demand results in 62.7% reduction of soot emissions from the engine, as well as a reduction of high current operation of the battery during propulsion. A decrease in high current operation leads to the lower temperature of the battery. Specifically, the battery temperature is 3 °C lower under the FDPD strategy than the baseline strategy. In addition, battery life is estimated by using the weighted Ah-processed model. The results show that the FDPD strategy can reduce the Ah-processed by 23% and thereby extend the battery lifespan over typical military driving conditions.

Future work will compare the FDPD strategy to optimal control strategies such as Dynamic Programming or Model-Predictive Control,

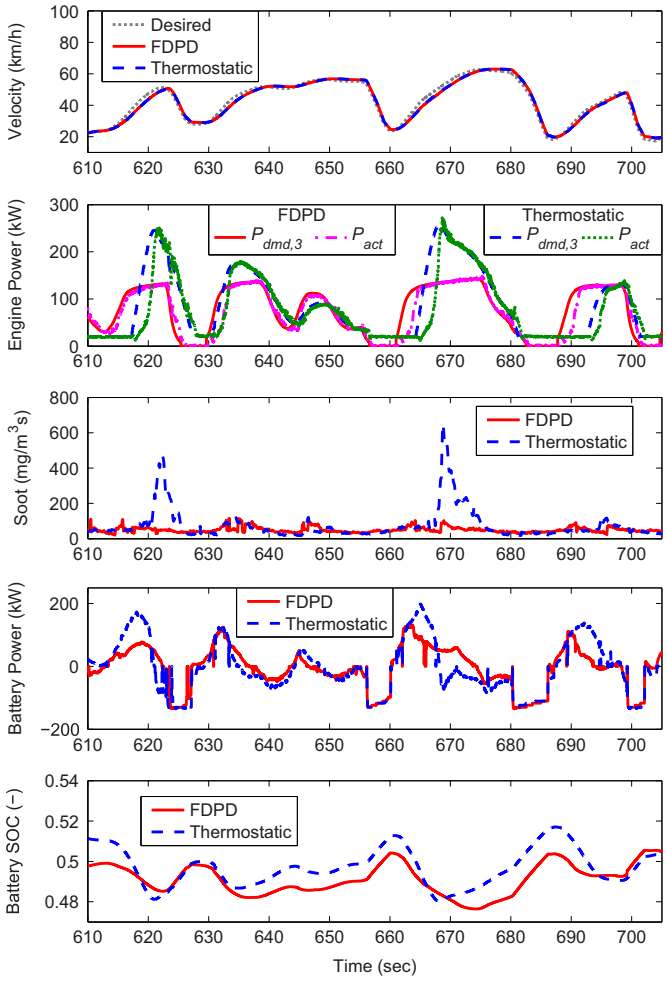

Fig. 9. Comparison of engine power demand, actual engine power, and soot emissions under different power management strategies. Soot emissions are measured from 0 to 750 s during the drive cycle since the electrometer detectors show drift when they are exposed to high concentrations for a long time period.

which requires the development of an accurate dynamic soot emissions model, and an efficient way of formulating and solving the resulting optimal control problem with increased dimensionality.

Acknowledgments

This work was supported by the Automotive Research Center (ARC), a U.S. Army Center of Excellence in Modeling and Simulation of Ground Vehicles.

Appendix A. SHEV modeling

This appendix presents the SHEV system model.

Fig. A1 shows the engine torque map obtained from a Navistar 6.4 L V8 diesel engine in Johri, Salvi, and Filipi (2012). The engine torque map is augmented by a PI fuel controller sub-model generating the engine rack position ($\zeta(t) \in [0,1]$), given by

$$\zeta(t) = k_P \Delta\tau_e + k_I \int \Delta\tau_e \, dt, \tag{A.1}$$

where $\Delta\tau_e$ is the error between the desired and actual engine torque; k_P and k_I are proportional and integral gains respectively. To represent the effect of turbocharger lag on transient response during rapid increases of engine rack positions, the fuel mass is filtered by a first order filter. The engine-generator unit is assumed to be fully warmed up so that the effects of temperature are ignored. Fig. A2 illustrates the efficiency of the generator obtained from Argonne National Laboratory (2002).

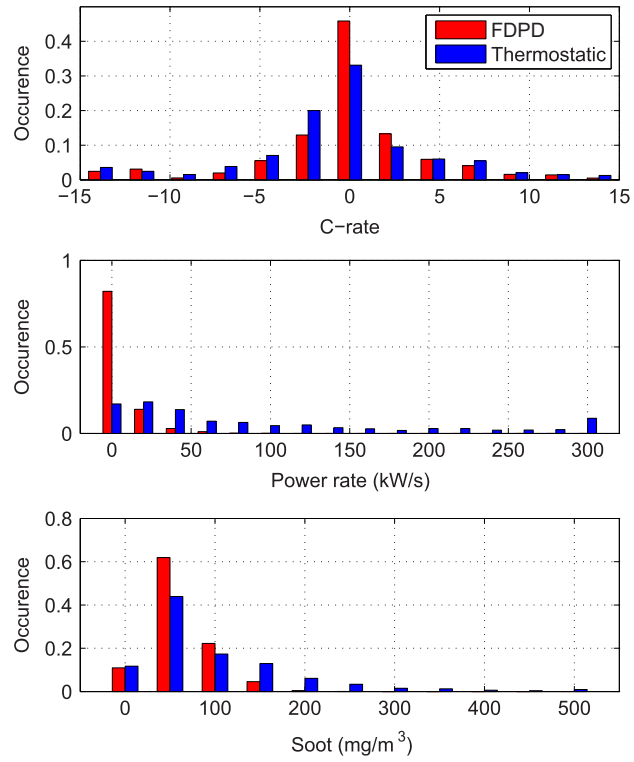

Fig. 10. Battery C-rate, engine power rate, and soot concentration histograms.

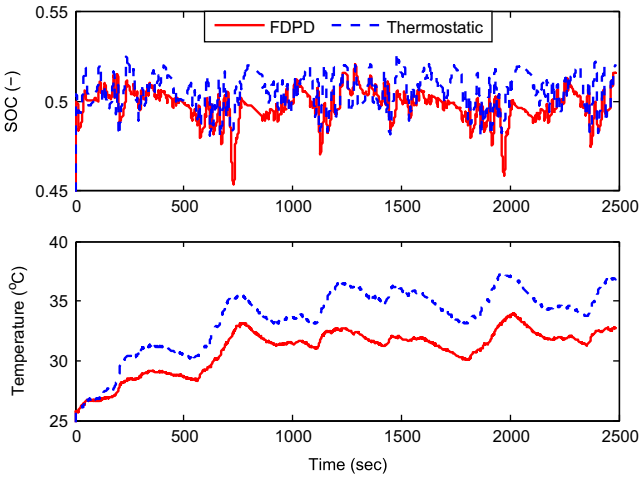

Fig. 11. Comparison of battery SOC and temperature under different power management strategies.

The most efficient operating points of the engine/generator combined system are different from the best engine-efficient operating points. In a series hybrid configuration, the attached generator possibly shifts the best fuel efficient operating points of the combined system to other operating points. The combined system brake specific fuel consumption (*bsfc*) map is obtained by dividing the engine *bsfc* map by the generator efficiency map. The *bsfc* of the engine/generator unit $bsfc_{eng/gen}$ can be calculated by using

$$bsfc_{eng/gen} = bsfc_{eng}/\eta_{gen}. \tag{A.2}$$

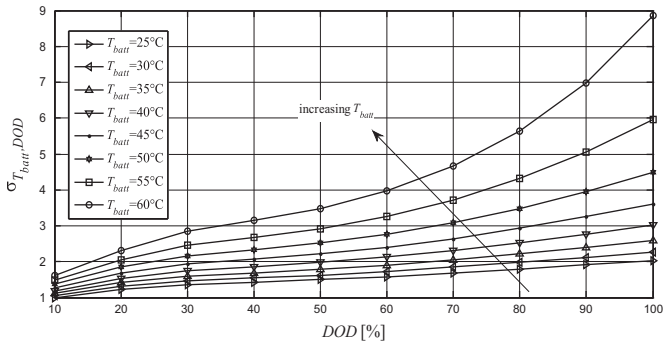

Fig. 12. Severity factor as a function of DOD parameterized with respect to battery temperature (Onori et al., 2012).

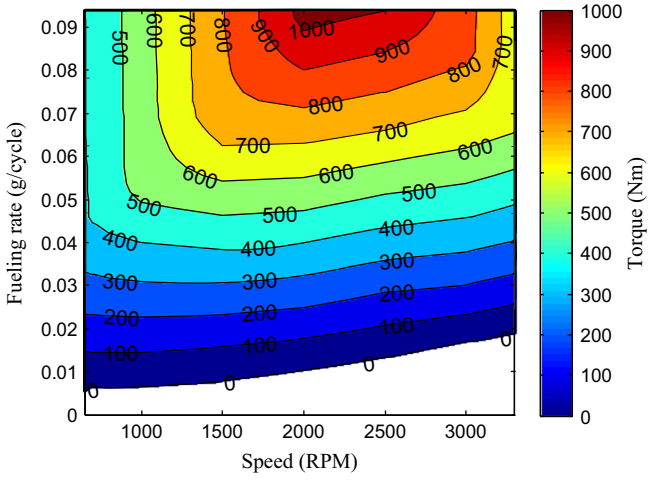

Fig. A1. Engine torque map as a function of speed and fuel rate.

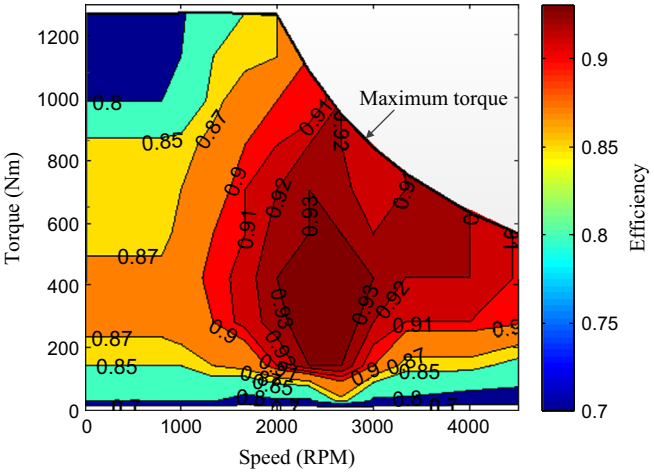

Fig. A2. Generator efficiency map as a function of speed and torque.

The best fuel-efficient operating line is then determined by searching the minimum fuel consumption point for any given power demand. Fig. A3 shows the combined $bsfc_{eng/gen}$ and optimal operation line of the engine/generator unit which is used for tuning both the thermostatic and FDPD strategies.

A 9.27 kWh (281 Ah) lithium ion battery pack with Lithium-Iron-Phosphate ($LiFePO_4$ or LFP) cells by A123 is considered and

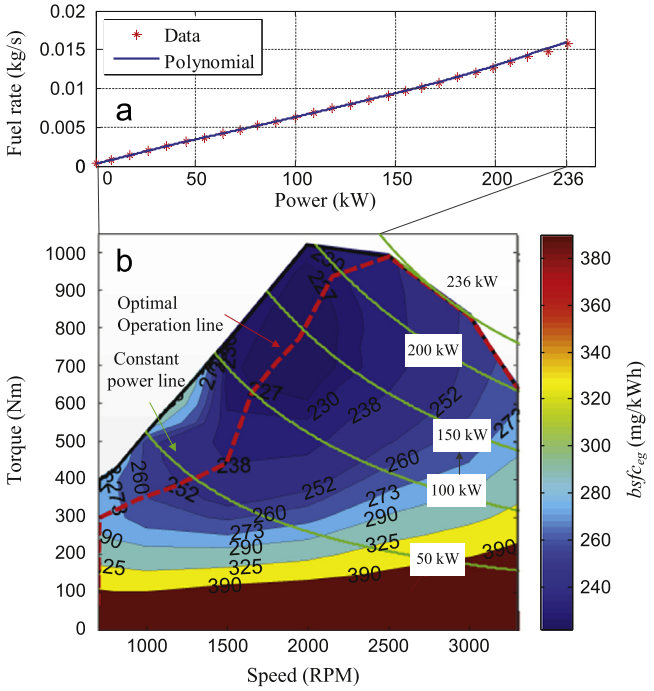

Fig. A3. *bsfc* of engine/generator unit obtained by combining engine *bsfc* and generator efficiency and superimposed by optimal operation lines of the engine/generator unit and the engine only.

Table A1
Specification of the battery.

Parameter	Value	Unit
Nominal voltage	3.3	V
Minimum voltage	2.0	V
Maximum voltage	3.6	V
Nominal capacity	2.3	Ah
Number of cells in series	130	–
Number of cells in parallel	10	–

the battery is modeled using an OCV-R-RC-RC equivalent circuit approach. This model has been parameterized and validated in Lin et al. (2014). The specifications for the LFP battery are summarized in Table A1.

Terminal voltage V_t of the battery is calculated by using

$$V_t = V_{oc} - V_1 - V_2 - IR_s, \tag{A.3}$$

where V_1 and V_2 are voltages across the capacitors C_1 and C_2, respectively, and calculated based on the following dynamic equations:

$$\frac{dV_i}{dt} = \frac{1}{C_i}\left(I - \frac{V_i}{R_i}\right), \quad i = 1, 2. \tag{A.4}$$

The sign convention is such that positive current denotes battery discharging.

Fig. A4 shows that the efficiency of the motor η_m is expressed as a function of motor torque τ_m and motor speed ω_m. Maximum output torque of the motor $\tau_{m,max}$ is governed between the continuous torque $\tau_{m,cont}$ and the peak torque $\tau_{m,peak}$ accounting for the heat index γ as follows:

$$\tau_{m,max} = \tau_{m,cont} + (1-\gamma)\tau_{m,peak},$$
$$\frac{d\gamma}{dt} = -\frac{0.3}{180}\left(\frac{\tau_m}{\tau_{m,cont}} - 1\right), \quad \gamma(0) = 0.3, \tag{A.5}$$

where $\tau_{m,cont}$ and $\tau_{m,peak}$ are a function of the motor speed ω_m as seen from Fig. A4. The heat index γ emulates the change in the torque limit

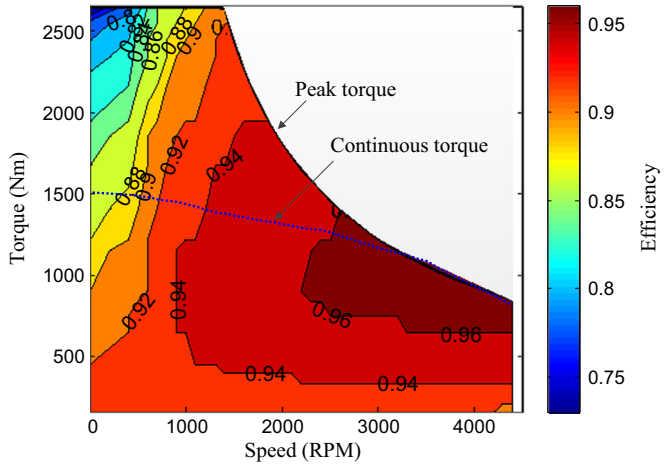

Fig. A4. Motor efficiency map superimposed by peak and continuous torques.

based on operating temperature as introduced in Powertrain Systems Analysis Toolkit (PSAT) developed by Argonne National Laboratory (2002).

A point-mass representation is used for the vehicle. The longitudinal dynamics of the vehicle is calculated through the equation

$$M_{\text{veh}}\frac{dv_{\text{veh}}}{dt} = F_{\text{prop}} - F_{\text{brk}} - F_{\text{RR}} - F_{\text{WR}}, \tag{A.6}$$

where M_{veh} is the mass of the vehicle, respectively, F_{prop} is the propulsion force, F_{brk} is the braking force, and F_{RR} is the rolling resistance force expressed by

$$F_{\text{RR}} = f_r M_{\text{veh}} a_g, \tag{A.7}$$

where f_r is the rolling resistance, and a_g is the gravitational acceleration. The wind resistance force F_{WR} is calculated by using

$$F_{\text{WR}} = \tfrac{1}{2}\rho_{\text{air}} C_d A_{\text{veh}} v_{\text{veh}}^2, \tag{A.8}$$

where ρ_{air} is the air density, C_d is the drag coefficient, and A_{veh} is the frontal area of the vehicle. The road grade is not considered in the driving cycles in this study.

The driver model, which takes the desired and actual vehicle velocities as inputs and provides propulsion or braking power demands, is adopted from Ersal et al. (2011) and is a PI controller with saturation and anti-windup.

References

Argonne National Laboratory, 2002. *Powertrain systems analysis toolkit* [Online; accessed 18-April-2014]. ⟨http://www.transportation.anl.gov/modeling_simulation/PSAT/⟩.

Assanis, D., Delagrammatikas, G., Fellini, R., Filipi, Z., Liedtke, J., Michelena, N., et al. (1999). Optimization approach to hybrid electric propulsion system design. *Mechanics of Structures and Machines*, *27*(4), 393–421.

Caratozzolo, P., Serra, M., & Riera, J. (2003). Energy management strategies for hybrid electric vehicles. In *Proceedings of the IEEE international electric machines and drives conference* (Vol. 1, pp. 241–248).

Di Cairano, S., Liang, W., Kolmanovsky, I. V., Kuang, M. L., & Phillips, A. M. (2012). Power smoothing energy management and its application to a series hybrid powertrain. *IEEE Transactions on Control Systems Technology*, *21*(6), 2091–2103.

Ersal, T., Brudnak, M., Salvi, A., Stein, J. L., Filipi, Z., & Fathy, H. K. (2011). Development and model-based transparency analysis of an internet-distributed hardware-in-the-loop simulation platform. *Mechatronics*, *21*(1), 22–29.

Ersal, T., Brudnak, M., Stein, J. L., & Fathy, H. K. (2012). Statistical transparency analysis in internet-distributed hardware-in-the-loop simulation. *IEEE/ASME Transactions on Mechatronics*, *17*(2), 228–238.

Ersal, T., Gillespie, R. B., Brudnak, M., Stein, J. L., & Fathy, H. (2013). Effect of coupling point selection on distortion in internet-distributed hardware-in-the-loop simulation. *International Journal of Vehicle Design*, *61*, 67–85.

Filipi, Z., Fathy, H., Hagena, J., Knafl, A., Ahlawat, R., Liu, J., et al. (2006). *Engine-in-the-loop testing for evaluating hybrid propulsion concepts and transient emissions – HMMWV case study*. SAE Technical Paper (2006-01-0443).

Filipi, Z., & Kim, Y. J. (2010). Hydraulic hybrid propulsion for heavy vehicles: *Combining the simulation and engine-in-the-loop techniques to maximize the fuel economy and emission benefits. Oil & Gas Science and Technology – Revue d'IFP Energies nouvelles*, *65*(1), 155–178.

Gao, W., & Porandla, S. (2005). Design optimization of a parallel hybrid electric powertrain. In *Proceedings of the IEEE vehicle power and propulsion conference* (pp. 530–535).

Hagena, J. R., Assanis, D. N., & Filipi, Z. S. (2011). Cycle-resolved measurements of in-cylinder constituents during diesel engine transients and insight into their impact on emissions. *Proceedings of the Institution of Mechanical Engineers, Part D: Journal of Automobile Engineering 225*(9), 1103–1117.

Holmstrom, K. (1989). *gclsolve.m: A standalone version of Direct*. Software documentation, revision 2.00. Sweden: HKH MatrisAnalys AB.

Jalil, N., Kheir, N., & Salman, M. (1997). A rule-based energy management strategy for a series hybrid vehicle. In *Proceedings of the American control conference* (Vol. 1, pp. 689–693).

Johri, R., Salvi, A., & Filipi, Z. (2012). Real-time transient soot and NO_x virtual sensors for diesel engine using neuro-fuzzy model tree and orthogonal least squares. *Journal of Engineering for Gas Turbines and Power*, *134*(9), 092806.

Jones, D., Perttunen, C., & Stuckman, B. (1993). Lipschitzian optimization without the Lipschitz constant. *Journal of Optimization Theory and Applications*, *79*(1), 157–181.

Kim, Y., Ersal, T., Salvi, A., Stefanopoulou, A. G., & Filipi, Z. (2012). Engine-in-the-loop validation of a frequency domain power distribution strategy for series hybrid powertrains. In *Proceedings of the IFAC workshop on engine and powertrain control simulation and modeling* (pp. 432–439).

Kim, Y., & Filipi, Z. (2007). *Simulation study of a series hydraulic hybrid propulsion system for a light truck*. SAE Technical Paper (2007-01-4151).

Kim, Y., Lee, T. K., & Filipi, Z. (2012). Frequency domain power distribution strategy for series hybrid electric vehicles. *SAE International Journal of Alternative Powertrains*, *1*(1), 208–218.

Kim, Y., Mohan, S., Siegel, J. B., Stefanopoulou, A. G., & Ding, Y. (2014). The Estimation of Temperature Distribution in Cylindrical Battery Cells Under Unknown Cooling Conditions. *IEEE Transactions on Control Systems Technology*, http://dx.doi.org/10.1109/TCST.2014.2309492.

Konev, A., Lezhnev, L., & Kolmanovsky, I. (2006). *Control strategy optimization for a series hybrid vehicle*. SAE Technical Paper (2006-01-0663).

Lave, L. B., & MacLean, H. L. (2002). An environmental-economic evaluation of hybrid electric vehicles: *Toyota's prius vs. its conventional internal combustion engine corolla. Transportation Research Part D: Transport and Environment*, *7*(2), 155–162.

Lee, T. K., Kim, Y., Stefanopoulou, A., & Filipi, Z. (2011). Hybrid electric vehicle supervisory control design reflecting estimated lithium-ion battery electrochemical dynamics. In *Proceedings of the American control conference* (pp. 388–395).

Li, D., & Feng, D. (2012). Thermostatic control for series hydraulic hybrid vehicle (shhv) energy management. *Advanced Materials Research*, *512–515*, 2676–2681.

Li, Y., & Kar, N. (2011). Advanced design approach of power split device of plug-in hybrid electric vehicles using dynamic programming. In *Proceedings of the IEEE vehicle power and propulsion conference* (pp. 1–6).

Lin, X., Perez, H. E., Mohan, S., Siegel, J. B., Stefanopoulou, A. G., Ding, Y., & Castanier, M. P. (2014). A lumped-parameter electro-thermal model for cylindrical batteries. *Journal of Power Sources*, *257*, 1–11, http://dx.doi.org/10.1016/j.jpowsour.2014.01.097.

Liu, J., Hagena, J., Peng, H., & Filipi, Z. S. (2008). Engine-in-the-loop study of the stochastic dynamic programming optimal control design for a hybrid electric HMMWV. *International Journal of Heavy Vehicle Systems*, *15*(2–4), 309–326.

Liu, J., & Peng, H. (2008). Modeling and control of a power-split hybrid vehicle. *IEEE Transactions on Control Systems Technology*, *16*(6), 1242–1251.

Michel, P., Charlet, A., Colin, G., Chamaillard, Y., Bloch, G., Nouillant, C., et al. (2013). *Pollution constrained optimal energy management of a gasoline-hev*. SAE Technical Paper (2013-24-0083).

Murphey, Y., Park, J., Chen, Z., Kuang, M., Masrur, M., & Phillips, A. (2012). Intelligent hybrid vehicle power control – part I: *Machine learning of optimal vehicle power. IEEE Transactions on Vehicular Technology*, *61*(8), 3519–3530.

Murphey, Y., Park, J., Kiliaris, L., Kuang, M., Masrur, M., Phillips, A., et al. (2013). Intelligent hybrid vehicle power control – part II: *Online intelligent energy management. IEEE Transactions on Vehicular Technology*, *62*(1), 69–79.

Onori, S., Spagnol, P., Marano, V., Guezennec, Y., & Rizzoni, G. (2012). A new life estimation method for lithium-ion batteries in plug-in hybrid electric vehicles applications. *International Journal of Power Electronics*, *4*(3), 302–319.

Pisu, P., & Rizzoni, G. (2005). A supervisory control strategy for series hybrid electric vehicles with two energy storage systems. In *Proceedings of the IEEE vehicle power and propulsion conference* (pp. 65–72).

Ramasamy, A., Hill, A. M., Hepper, A. E., Bull, A. M. J., & Clasper, J. C. (2009). Blast mines: *Physics injury mechanisms and vehicle protection. Journal of the Royal Army Medical Corps*, *155*(4), 258–264.

Reavell, K., Hands, T., & Collings, N. (2002). *A fast response particulate spectrometer for combustion aerosols*. SAE Technical Paper (2002-01-2714).

Serrao, L., Onori, S., Rizzoni, G., & Guezennec, Y. (2009). A novel model-based algorithm for battery prognosis. In *Proceedings of the IFAC symposium on fault detection, supervision and safety of technical processes*.

Serrao, L., Onori, S., Sciarretta, A., Guezennec, Y., & Rizzoni, G. (2011). Optimal energy management of hybrid electric vehicles including battery aging. In *American control conference* (pp. 2125–2130).

Serrao, L., Sciarretta, A., Grondin, O., Chasse, A., Creff, Y., Di Domenico, D., et al. (2013). Open issues in supervisory control of hybrid electric vehicles: *A unified approach using optimal control methods. Oil & Gas Science and Technology – Revue d'IFP Energies nouvelles*, *68*(1), 23–33.

Yang, S., Qi, C., Guo, D., Wang, Y., & Wei, Z. (2012). Topology optimization of a parallel hybrid electric vehicle body in white. *Applied Mechanics and Materials*, *148–149*, 668–671.